

UC Davis

UC Davis Previously Published Works

Title

3D nanoprinting via spatially controlled assembly and polymerization

Permalink

<https://escholarship.org/uc/item/7cz8q4s0>

Journal

Nature Communications, 13(1)

ISSN

2041-1723

Authors

Pattison, Thomas G

Wang, Shuo

Miller, Robert D

et al.

Publication Date

2022

DOI



10.1038/s41467-022-29432-z

Copyright Information

This work is made available under the terms of a Creative Commons Attribution License, available at <https://creativecommons.org/licenses/by/4.0/>

Peer reviewed

3D nanoprinting via spatially controlled assembly and polymerization

Thomas G. Pattison ¹, Shuo Wang², Robert D. Miller³, Gang-yu Liu ²✉ & Greg G. Qiao ¹✉

Macroscale additive manufacturing has seen significant advances recently, but these advances are not yet realized for the bottom-up formation of nanoscale polymeric features. We describe a platform technology for creating crosslinked polymer features using rapid surface-initiated crosslinking and versatile macrocrosslinkers, delivered by a microfluidic-coupled atomic force microscope known as FluidFM. A crosslinkable polymer containing norbornene moieties is delivered to a catalyzed substrate where polymerization occurs, resulting in extremely rapid chemical curing of the delivered material. Due to the living crosslinking reaction, construction of lines and patterns with multiple layers is possible, showing quantitative material addition from each deposition in a method analogous to fused filament fabrication, but at the nanoscale. Print parameters influenced printed line dimensions, with the smallest lines being 450 nm across with a vertical layer resolution of 2 nm. This nanoscale 3D printing platform of reactive polymer materials has applications for device fabrication, optical systems and biotechnology.

¹Polymer Science Group, Department of Chemical Engineering, The University of Melbourne, Parkville, VIC 3010, Australia. ²Department of Chemistry, University of California, Davis, CA 95616, USA. ³International Business Machines—Almaden Research Center, 650 Harry Road, San Jose, CA 95120, USA. ✉email: gylu@ucdavis.edu; gregghq@unimelb.edu.au

Three-dimensional (3D) printing has revolutionized manufacturing and prototyping^{1–3}, but its translation to the bottom-up, continuous formation of soft materials at the nanoscale remains a significant challenge primarily due to the difficulties in delivering the minute amounts of materials required with nanometer precision. A successful, robust 3D nanoprinting platform must address several critical design parameters such as a high degree of control over the spatial deposition of material, a continuous printing nature with minimal to no intermediate steps to stabilize printed layers without loss of feature registry between printing steps, and the deposition of solvent-free material to reduce or eliminate shrinking from solvent loss and enable the creation of multilayered features.

Herein, we report a 3D nanoprinting platform that enables the printing of polymer materials by design and with nanometer spatial precision. The approach combines the spatial precision of an atomic force microscope (AFM), the accurate materials delivery of a microfluidic probe^{4–6}, and the rapid curing using our solid-state continuous assembly and polymerization (CAP)⁷. A surface-initiated ring-opening metathesis reaction was used to bind a reactive ink, e.g., a solventless polymer, to the surface. This “ink” was delivered directly to the substrate using microfluidic AFM probes. With the surface functionalized by our chosen initiator and catalyst, the polymer was assembled and crosslinked immediately upon delivery. The exposed surface always remained functionalized due to the living nature of our chosen reactions. The amount of polymer delivered was controlled via our microfluidic AFM system by controlling the delivery conditions, e.g., pressure, speed, and contact time. The AFM allowed accurate movement by designed trajectory with nanometer precision. Therefore, this combination enabled the concept of 3D nanoprinting. In comparison with prior attempts of 3D nanoprinting using metallization^{8–11} or molecular assembly^{12–14}, this approach can be applied to a wide range of polymer materials, exhibits high spatial accuracy and fidelity to design due to the rapid assembly and polymerization upon delivery. In contrast to conventional 3D printing which often uses thermal melting and solidifying during cooling^{15–17}, our reactions of curing occur at room temperature, with faster curing time and higher product stability.

To develop a nano-3D printing platform that could create polymer features in a continuous fashion, we used the Continuous Assembly of Polymers technique (CAP) to form stable structures. The CAP method uses polymer macrocrosslinkers containing crosslinking pendants that form highly crosslinked surface-tethered polymer films via surface-initiated polymerization (SIP), while maintaining a high degree of chemical tailorability via the remaining polymer side group functionality. This polymer is then delivered to a substrate initiated with surface-tethered catalyst molecules where the pendant monomer groups on the macro-crosslinker undergo SIP in the solid state⁷, covalently binding the macrocrosslinkers to the surface. A variety of SIP methods^{18,19} have been shown to work with CAP^{20–22}, but typically require similar degrees of deoxygenation and reagent purification to the analogous SIP in order to successfully form crosslinked material²³. Ring-opening metathesis polymerization (ROMP) using the catalyst Grubbs Generation III has shown tolerance to moisture and oxygen²⁴, which is compatible with our 3D nanoprinting setup. However, even with the aforementioned advances, it is still difficult to perform commonly known surface-initiated ROMP successfully in air, as the catalyst typically undergoes degradation in ambient conditions^{25,26}. To do so, our catalyzed surfaces were used immediately after initiation to prevent excessive degradation of the activated surface groups: substrates that have been modified with silane but yet to be exposed to Grubbs catalyst can be kept in inert atmospheres for at least up to 2 weeks and still yield cross-linked structures after activation with catalyst.

To achieve the microfluidic delivery of viscous material layer-by-layer¹², a new and highly reactive random co-polymer was designed (Fig. 1A, poly(poly(ethylene glycol acrylate-co-hydroxyethylacrylate norbornene), p(PEGA-co-HEANB)) which undergoes ROMP-based crosslinking without the presence of solvent and in a rapid fashion before significant catalyst degradation. To do so, hydroxyethylacrylate and oligoethylene glycol monomethyl ether acrylate were copolymerized, and the product was functionalized post-polymerization to add highly reactive exo-norbornenyl pendants^{27–29} to the co-polymer, resulting in the crosslinkable p(PEGA-co-HEANB). Acrylates and oligo/poly(ethylene glycol)-based materials have been widely used in a variety of biological applications, including the formation of crosslinked hydrogel materials^{30–32}. The glass transition temperature of the polymer being $-52\text{ }^{\circ}\text{C}$ (Supplementary Figures 2–4) enabled the polymer to be printed as a viscous liquid at room temperature, avoiding issues with using solvent such as excessive material spreading and evaporation at the printing aperture. To facilitate the surface-initiated crosslinking upon delivery of polymer inks, quartz wafers were functionalized with [(5-bicyclo[2.2.1]hept-2-enyl)ethyl]methyl-dichlorosilane according to a previously published procedure³³, as illustrated in Fig. 1B. After functionalization, the wafers were exposed to a solution of 3rd generation Grubbs catalyst to anchor the metathesis catalyst to the surface, creating initiating sites for the ROMP reaction. The excess physisorbed catalyst was removed from the surface via repeated solvent washing before being blown dry with N_2 . Reactivity of the synthesized ink was tested by spin-coating a solution of the polymer onto a silanized and initiated substrate (Fig. 1B) allowing the polymer to crosslink via surface-initiated ROMP. After 12 hours of reaction time, the film was washed to remove any un-crosslinked material, revealing a stable film 400 nm thick on the surface. Due to the living nature of the crosslinking ROMP reaction, further material can be added and is crosslinked by terminal catalyst species present at the surface of previously cross-linked polymer.

To spatially control the delivery of macrocrosslinkers (or polymer inks) to the pre-functionalized surface, an integrated AFM and microfluidic probe were used, referred to as FluidFM BOT (Fig. 1C). The neat p(PEGA-co-HEANB) liquid was loaded into the probe. The amount of material delivered to the surfaces was controlled by varying the probe-surface contact (AFM load), microfluidic pressure, and printing speed (or transient contact time). The system enabled delivery volumes as small as 0.5 aL⁵. The movement precision reached 5 nm over 1 mm range¹². As a minute amount of p(PEGA-co-HEANB) was delivered to the designed location, the CAP crosslinking occurred immediately to solidify the ink, while the catalyst migrated to the outmost surface of the printed feature (Fig. 1B, C) to enable living CAP during subsequent printing. These observations demonstrate that the printing of multiple layers was accomplished without the need to reinitiate the previously deposited material—as no loss of catalyst activity was observed for at least 70 mins after deposition on surfaces in ambient conditions. Once lines were deposited and printing was finished, the substrates with printed structures were rinsed with dichloromethane (DCM) with 5% ethyl vinyl ether (EVE, to terminate the crosslinking), placed in 5% EVE in DCM for 1 hour, and then washed again with fresh DCM before placing under vacuum overnight prior to analysis via AFM.

Results and discussion

Surface-initiated 3D nanoprinting. The concept of our 3D nanoprinting based on CAP was first demonstrated by printing an array of three polymer lines on a ROMP-active quartz surface. The lines were parallel with interline separation of 5 μm . As shown in Fig. 2A, these lines were identical in size and measured

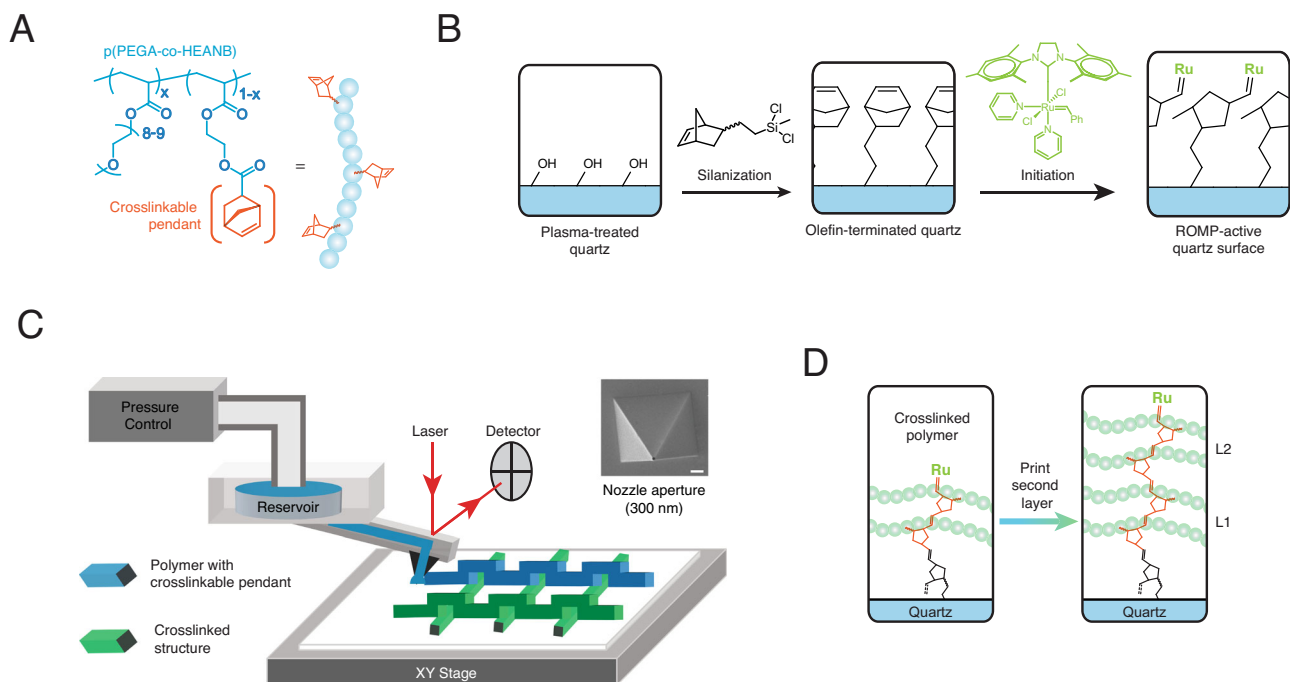


Fig. 1 Schematic diagrams illustrating key steps in our 3D nanoprining, including chemical crosslinking ink, surface modification and initiation, and the delivery of reactive ink to substrates to form 3D printed patterns. **A** Structural formula of the crosslinking polymer, poly(poly(ethylene glycol) acrylate-co-hydroxyethylacrylate norbornene (p(PEGA-co-HEANB)), highlighting the crosslinkable pendant groups in orange. **B** Pre-functionalization of the surfaces with olefin-terminated SAM and initiated with the ROMP (ring-opening metathesis polymerization) catalyst Grubbs Generation III to enable Continuous Assembly of Polymers (CAP) upon delivery of p(PEGA-co-HEANB). **C** Schematic diagram illustrating the combined atomic force microscope (AFM) with microfluidic delivery, in realizing the CAP upon printing. The green material on the substrate shows crosslinked structures, while the blue is yet to be crosslinked. The inset scanning electron microscope image is of a FluidFM Nanopipette with a 300 nm aperture. Courtesy of Cytosurge AG. **D** Schematic of the resulting crosslinking formed after two layers of polymer have been deposited, showing the ability of the catalyst to continue crosslinking material. SEM scale bar: 2 μm .

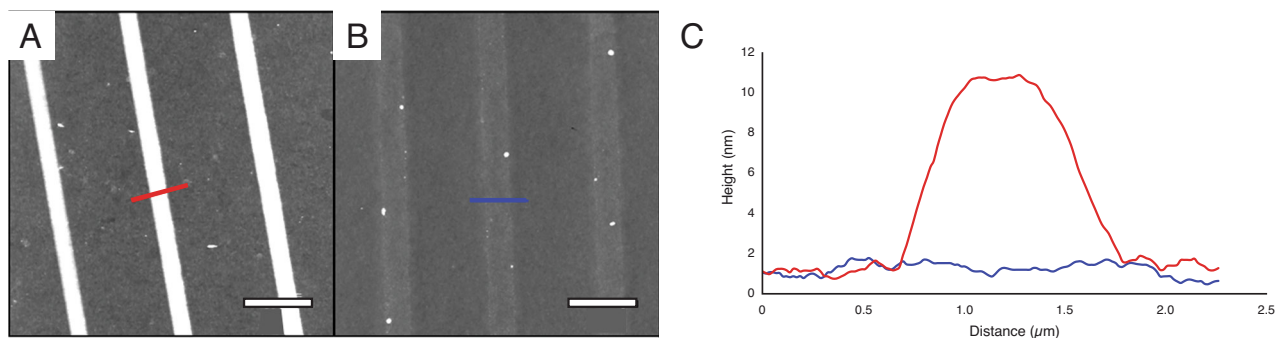


Fig. 2 Atomic force microscopy images of 3D nano-printed line arrays using spatially controlled assembly and polymerization from initiated substrates as well as control substrates, demonstrating the active crosslinking reaction. **A** 15 $\mu\text{m} \times 15 \mu\text{m}$ AFM topographic image of an array of the crosslinked polymer lines on a ROMP-active quartz surface. **B** 15 $\mu\text{m} \times 15 \mu\text{m}$ AFM topographic image of an array of lines printed with the same protocol as **A** without the catalyst present on a quartz surface. **C** Combined cursor profile from the two cursors indicated in **A** (red) and **B** (blue). Scale bars = 3 μm .

11 nm tall and 1.7 μm wide, and 100 μm long. Under identical conditions and using a clean quartz substrate without catalyst, control experiments were carried out. As shown in Fig. 2B, minimal p(PEGA-co-HEANB) assembly or cross-linking occurred. Figure 2C compares the AFM trace of the crosslinking system vs. the non-initiated control experiment (no catalyst), clearly showing the much taller line formed by the nano-3D printing system (11 nm) than that in the control (0.6 nm). The robustness of the observations was proven by printing larger features using a “micropipette” with 4 μm pore. An array of four lines, 300 μm long, were produced, each was 60 nm tall with the base width ranging from 10 to 25 μm (Supplementary Figure 5). In contrast,

control experiments did not yield any polymer lines. These tests confirm that assembly and catalyst-initiated crosslinking occurred during printing processes, i.e., spatially controlled CAP was the mechanism in our 3D nanoprining.

Influence of parameters on printed dimensions. We could easily tune the printed line dimensions such as width and height by changing the printing parameters. Quantitative correlation between delivery parameters and liquid volume could be estimated using fluid dynamics approaches. A common example is derivations based on the Cox-Voinov equation using geometric

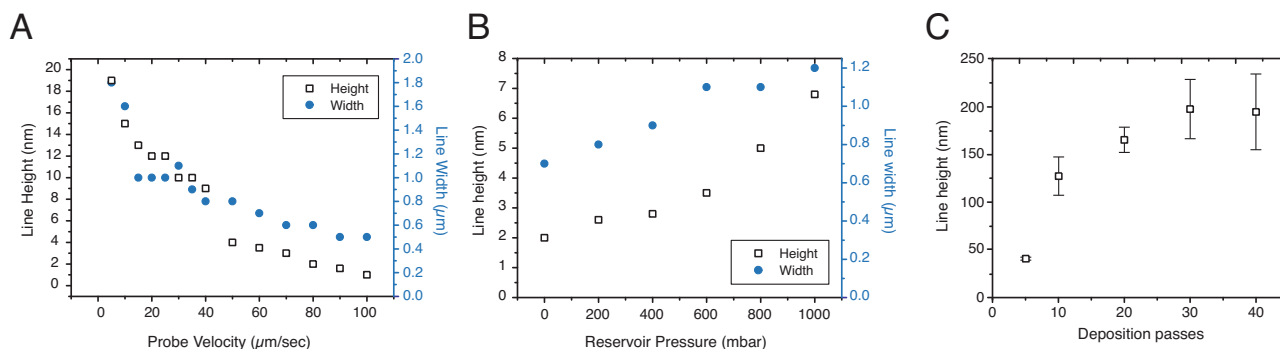


Fig. 3 Data showing the influence of various printing parameters on the dimensions of the final printed lines. **A** A plot showing the changes in the dimension of polymer lines with increasing printing speed, at 200 mbar. **B** A plot showing the variation of the dimension of polymer lines with increasing reservoir pressure, at the constant speed of 10 μm/sec. **C** Height of printed lines constructed after a designed number of passes and rinsing with a good solvent, error bars are st. dev. (where $n = 3$).

approximations^{34,35}; another example is the energy balance to quantify the deposition process for macroscopic fluid delivery³⁶. Before each experiment, we performed our own calibration⁵ to correlate delivery parameters and delivered volume to address variations between individual tip apertures. The molecular assembly under spatial confinements was modeled and discussed in our prior work⁵. For materials used in this work, Fig. 3A, B shows that the line width and height could be varied by changing the printing speed and pressure. Under constant reservoir pressure, the extrusion rate of polymer is constant, thus the height of the line increased with the decreasing printing speed along the line, as demonstrated in Fig. 3A. Decreasing speed is equivalent to longer transient time, thus more material is extruded and available for crosslinking over a given distance. At 100 μm/sec and 200 mbar, the lines height and width were 1 nm and 400 nm, respectively. Much taller lines were produced by decreasing the printing speed—for example, at 5 μm/sec, lines are 19 nm tall and 1.85 μm wide. Increasing the printing pressure resulted in more material being extruded through the probe aperture per second and therefore a wider and taller line, as shown in Fig. 3B. Deposition was also observed at 0 mbar of reservoir pressure, likely due to the capillary action of the polymer through the aperture.

We also investigated the activity of the catalyst by depositing lines with an increasing number of passes, and then rinsing the surface to reveal stable polymer. When printing with the 300 nm aperture tip at 10 μm/sec and 1000 mbar of reservoir pressure, an increase in line-height was observed up to 30 depositions. Beyond this, the line height did not decrease. This corresponded with a line-height of 200 nm and indicates the burying of catalyst within the printed structure so that it can no longer crosslink further depositions without additional reinitiations. These results align with findings that were demonstrated with the CAP system in our previous work³³.

In comparison with optical-based 3D-printing methods such as two-photon direct laser writing, microstereolithography, and volumetric additive manufacturing (VAM), our approach, although slower in terms of printing speed, enables broader applications as we could print various materials without being restricted to using materials that contain photosensitive or photoactive molecules. Thus, this methodology could save time overall, as it reduces the time required to synthesize molecules containing photoactive functional groups, and in the preparation of photolithography such as formulating the crosslinking mixture and solubilizing photoinitiator, or pre-baking a photoresist layer. In addition, individual z-layer precision in this method is ~2 nm (single layer), which is much thinner (or high precision) than

what is typically achievable using optical-based 3D printing, these processes are usually limited by the diffraction limit (half of the wavelength). In comparison to other scanning probe microscopy (SPM) based nanolithography methods such as dip-pen nanolithography (DPN)^{37–40}, and nanografting^{41,42}, the spatial precision (in nanometers) is similar during the production of the first layer. The typical speed of SPM methods is 1–100 μm/s, and our approach can reach 1 mm/s¹². These single probe methods have been scaled through the use of parallel arrays^{43,44}. In terms of 3D nanoprinting by design, only our approach enables layer-by-layer delivery of materials by design.

3D nanoprinting of structures. The capability to print 3D structures by design was also demonstrated, with representative 3D structures shown in Fig. 4. The first structure is a set of stacked grids: an array of 10 parallel lines, 100 μm long with 10 μm separation, were printed atop a pre-functionalized quartz surface. Then the same printing protocols were followed by delivering 10 lines of p(PEGA-co-HEANB) atop and perpendicular to the first array. As shown in Fig. 4A the outcome exhibited high fidelity when compared to the design, with completely parallel lines separated by designed periodicity and perpendicularity from one array to the next without distortion or fuzzy edges. The height of lines measured to be 26 and 34 nm, for the first and second arrays, respectively, as shown in Fig. 4B. The cross-section was 60 nm tall, consistent with the concept of stacking individually printed passes on top of one another and is shown more clearly in the 3D image in Fig. 4C. The printing of multiple layers of a square pattern one after another is shown in Fig. 4D. The structure was created by printing 10 consecutive squares atop each other with 30 μm side length. The resulting structure shows a 3D square with walls of 98 ± 12 nm in height and 2.3 ± 0.3 μm in width, showing that the continuous deposition of materials enables the formation of taller features when compared to a single deposition, with minimal distortion in the final structure. Another 3D structure demonstrated was the stacking of cuboids (Fig. 4E) atop one another, whose designed dimensions are summarized in Table 1. The base was a cuboid with designed dimensions of 40 μm × 40 μm × 40 nm. Stacking atop this cuboid was a smaller cuboid with 20 μm × 20 μm × 15 nm. At the top were four cones designed to be 15 nm tall and 400 nm wide. As shown in Fig. 4E and outlined in Table 1, the outcome faithfully followed the design. The base cuboid measured as 42.1 ± 1.6 μm × 41.2 ± 1.5 μm in lateral dimensions and 61 ± 5 nm tall, produced by printing 133 lines at 300 nm separation. The next cuboid atop of the center region of the base measured 21.5 ± 1.3 μm × 20.8 ± 1.4 μm × 15 ± 2 nm created by

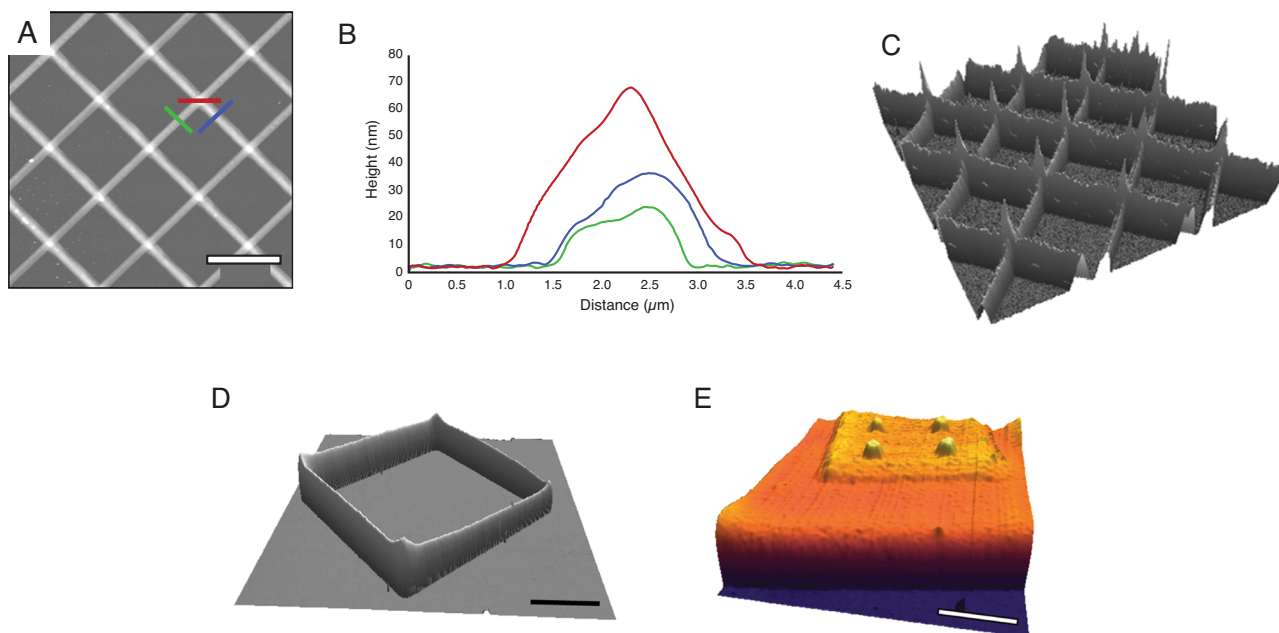


Fig. 4 Atomic force microscopy of 3D nanoprinting following designed structures, highlighting the ability to form multilayered patterns atop of printed material. **A** $40\ \mu\text{m} \times 40\ \mu\text{m}$ AFM topographic image of the printed cross-grids of crosslinked polymer. **B** Combined cursor profiles from three colored cursors indicated in **A**. **C** A 3D display of **A** with z scale 0–80 nm. **D** A 3D display of a $50\ \mu\text{m} \times 50\ \mu\text{m}$ AFM topographic image of the 3D square structure with z scale 0–150 nm. **E** A 3D display of a $35\ \mu\text{m} \times 35\ \mu\text{m}$ AFM topographic image of stacked cuboids with z scale 0–120 nm. Scale bar in **A**, **D**, and **E**: $10\ \mu\text{m}$.

Table 1 Design and geometries of the printed feature in Fig. 4E.

Geometry	Designed width (μm)	Number of lines	Designed separation (μm)	Measured width (μm)	Measured layer height (nm)
Bottom cuboid	40	133	0.3	$42.1 \pm 1.6 \times 41.2 \pm 1.5$	61 ± 5
Middle cuboid	20	40	0.5	$21.5 \pm 1.3 \times 20.8 \pm 1.4$	15 ± 2
Top 4 cones	0.4	4	8	0.34 ± 23	17 ± 2

printing 40 lines with 500 nm separation. The four cones are located at the center of the four quadrants atop the second cuboid. Each cone was produced by dispensing a droplet of liquid polymer with a contact time of 1 s under 200 mbar delivery pressure. The dimensions of the cones measured $340 \pm 23\ \text{nm}$ at the base and $17 \pm 2\ \text{nm}$ tall. The capability of printing 3D structures by design has been demonstrated by other designs and using a variety of probes (Supplementary Figure 5). In all cases, the neat polymer ink crosslinked rapidly and maintained its stability for a minimum of 7 days. Additionally, depositing atop of this structure through the delivery of neat polymer does not alter the cured structures underneath. These observations further prove that our approach and materials enabled 3D nanoprinting by design.

Conclusion

In conclusion, we have demonstrated a generic 3D printing method for creating stable three-dimensional micro- and nanostructures of polymeric materials by design. Using a scanning probe microscopy-based technology, the reactive ink materials are directly delivered to the localized site following the designed trajectory. Through a rapid SIP to form crosslinks, the delivered polymer ink is cured rapidly on surface contact, resulting in high fidelity of the 3D design. The living nature of our crosslinking reactions allows for continuous printing without requiring an additional application of catalyst or processing, resulting in truly continuous material delivery in multiple layers. High spatial selectivity and fidelity are achieved by varying printing parameters and the real-time control of the AFM-

nanofluidic platform. This approach is of generic importance in 3D nanoprinting of materials in general. Work is in progress to explore the feasibility and accuracy in 3D printing of other polymer materials such as block co-polymers, antibacterial materials, and nano-architected materials including star polymers. Work is in progress for further miniaturization and to enable the printing of overhanging features, which would require the curing rate to be faster than the rate of material delivery. The combination of smart polymer engineering with three-dimensional, bottom-up micro/nanofabrication fills the technology void of 3D nanoprinting, with potential for use in a myriad of applications such as stimuli-responsive optical coatings, customized polymer features in microfluidics such as actuators, and tailored polymer surfaces to study cell-material interactions.

Methods

Materials. DCM (99.8%) and tetrahydrofuran (THF, 99.9%) were received from J.T. Baker and were passed through a solvent purification tower to remove oxygen and moisture before use. Water was obtained from a Millipore MilliQ filtration system. Silicon wafers (1" diameter with native oxide) and quartz wafers (1" diameter) were purchased from Virginia Semiconductor, VA. [(5-bicyclo[2.2.1]hept-2-enyl)ethyl]methylchlorosilane (tech-95, endo/exo isomers, 95%) was obtained through Gelest and used as received. Exo-5-norbornene carboxylic acid (5-NB-COOH, 97%) was obtained from Sigma Aldrich and used as received. Poly-ethyleneglycol monomethyl ether acrylate (PEGA, 99.5%) was purchased from Sigma Aldrich and passed through a column of basic alumina to remove the inhibitor immediately before use. 2-Hydroxyethylacrylate (HEA, 98%) was distilled at reduced pressure immediately before use. Azobisisobutyronitrile (AIBN, 98%) was obtained from Sigma Aldrich and was recrystallized twice from methanol. Unless otherwise stated, all other compounds were used as supplied.

Wafer cleaning. Polished silicon wafers or transparent quartz wafers were cleaned of particulates by sonication in acetone for 20 mins and then exposed to a 45 s oxygen reactive ion etch (RIE) cycle, which removes any organic residue and exposes the native oxide silanol groups. The wafers were then immediately modified using the procedure below.

Silanization of quartz substrates. In an N₂-filled glove bag, clean, plasma-activated quartz wafers were exposed to a 2.8% solution of [(5-bicyclo[2.2.1]hept-2-enyl)ethyl]methylchlorosilane in anhydrous pentane for 6 hours. The silanized wafers were then sonicated for 5 minutes each in the following solvents: toluene, toluene/acetone (1:1), acetone for a total of 20 mins. They were then either used immediately for ssCAP_{ROMP} reactions or were stored under N₂ until use.

Attachment of catalyst to silanized quartz wafer. In an N₂ filled glove bag, a solution of 6.7 mg/mL of 3rd generation Grubbs catalyst was prepared in anhydrous THF. The solution was filtered through a 0.45 µm PTFE filter and a wafer silanized with the olefin-dichlorosilane was placed into the solution for 20 mins. The wafer was then rinsed once in anhydrous THF and twice in anhydrous DCM to remove the physisorbed catalyst before being exposed to polymer without delay.

Solid-state CAP_{ROMP} from catalyzed, silanized quartz surface. To test the polymer for surface-initiated crosslinking, the material was dissolved in dry THF to make a solution of 10 mg/mL before being spin-coated at 1200 RPM for 30 seconds, then held at 3000 RPM for 30 seconds before being placed in air or under N₂ for the requisite amount of time.

Quenching of the surface-initiated ROMP reaction. Substrates were removed from the vacuum drying oven or printing stage and were rinsed with copious amounts of THF/DCM before being rinsed in a container with neat EVE to remove the catalyst. The wafer was then rinsed once again with DCM before being vacuum dried for analysis.

Printing experiments. The printing process was performed using a FluidFM BOT (Cytosurge, Glattbrugg, Switzerland) containing an inverted optical microscope (IX-73, Olympus America, Center Valley, PA, USA). The xy-stage (Fig. 1C) was mounted onto an inverted optical microscope to monitor the position and delivery, with a lateral movement range of 240 mm × 74 mm, and a precision of 5 nm. The z-movement is independent of lateral movement with 4 nm precision over 50 mm. The substrate was placed on the xy-stage, while the probe was mounted to the vertical assembly controlling z-movement. The FluidFM Nanopipette or FluidFM Micropipette (CYPR/001511, Cytosurge, Glattbrugg, Switzerland) used for printing was integrated with a microfluidic delivery system. Typical probe-surface contact during delivery is shown in Fig. 1C, where the contact force was measured and controlled via similar means as conventional AFM with a deflection configuration. The square pyramidal tip-tilted 11° from the surface normal. The cantilever was similar to conventional AFM probes, 200 µm long, 36 µm wide, and 1.5 µm thick. The spring constant was 2 N/m. A typical nanopipette has a 300 nm diameter pore located at the probe apex, connected to a microchannel within. The microchannel was connected to a small reservoir where the polymer resided, and a mechanical pump and control system enabled the application of pressures from -800 mbar to +1000 mbar with 1 mbar precision. To print, the nanopipette was first filled with polymer by applying a high pressure (i.e., 1000 mbar) to allow the material to flow through the nanofluidic channel and fill the hollow section within the cantilever and tip. Hamilton 7000 series syringes, 1 µL (Hamilton, Reno, NV, USA), were used to deliver the printing material into the instrument's reservoir. Unless otherwise stated, typical printing parameters are: contact force = 40 nN, probe moving velocity = 10 µm/sec, and printing pressure = 200 mbar. Once the printing was completed, wafers were rinsed in solvent to remove any uncross-linked material, dried with a flow of nitrogen, and placed under vacuum to remove residual solvent before being characterized via AFM.

Atomic force microscopy. AFM images were acquired using a deflection type configuration (MFP-3D, Oxford Instrument, Santa Barbara, CA, USA). Probes (AC240-TS, Olympus America, Central Valley, PA, USA) of 1.7 N/m spring constant and 57 kHz resonant frequency were used to characterize the geometry and size of the printed structures. The driving frequency was set at the fundamental resonance of the cantilever, 57 kHz, and the damping was set at 40%. Image processing and display were performed using either the MFP-3D software developed on the Igor Pro 6.20 platform or Gwyddion (open-source software, Czech Metrology Institute, Brno, Czech Republic).

Data availability

The source data used in this study (used to generate Figs. 2C, 3A–C, and 4B) is available in the figshare database under accession code (<https://doi.org/10.6084/m9.figshare.17991482.v1>). Source data are provided with this paper.

Received: 6 May 2021; Accepted: 2 March 2022;

Published online: 11 April 2022

References

1. Bose, S., Vahabzadeh, S. & Bandyopadhyay, A. Bone tissue engineering using 3d printing. *Mater. Today* **16**, 496–504 (2013).
2. He, Y., Wu, Y., Fu, J., Gao, Q. & Qiu, J. Developments of 3D printing microfluidics and applications in chemistry and biology: a review. *Electroanalysis* **28**, 1658–1678 (2016).
3. Panwar, A. & Tan, L. Current status of bioinks for micro-extrusion-based 3D bioprinting. *Molecules* **21**, 685 (2016).
4. Meister, A. et al. FluidFM: combining atomic force microscopy and nanofluidics in a universal liquid delivery system for single cell applications and beyond. *Nano Lett.* **9**, 2501–2507 (2009).
5. Zhang, J. et al. Controlled molecular assembly via dynamic confinement of solvent. *J. Phys. Chem. Lett.* **9**, 6232–6237 (2018).
6. Zhang, J. et al. Direct observation of tunneling nanotubes within human mesenchymal stem cell spheroids. *J. Phys. Chem. B* **122**, 9920–9926 (2018).
7. Nam, E. et al. Continuous assembly of polymers via solid phase reactions. *Chem. Sci.* **5**, 3374–3380 (2014).
8. Hirt, L. et al. Template-free 3D microprinting of metals using a force-controlled nanopipette for layer-by-layer electrodeposition. *Adv. Mater.* **28**, 2311–2315 (2016).
9. Hirt, L., Reiser, A., Spolenak, R. & Zambelli, T. Additive manufacturing of metal structures at the micrometer scale. *Adv. Mater.* **29**, 1604211 (2017).
10. Frazier, W. E. Metal additive manufacturing: a review. *J. Mater. Eng. Perform.* **23**, 1917–1928 (2014).
11. Hirt, L. et al. Local surface modification via confined electrochemical deposition with FluidFM. *RSC Adv.* **5**, 84517–84522 (2015).
12. Ventrici de Souza, J. et al. Three-dimensional nanoprinting via direct delivery. *J. Phys. Chem. B* **122**, 956–962 (2018).
13. Fang, A., Dujardin, E. & Ondařchuh, T. Control of droplet size in liquid nanodispensing. *Nano Lett.* **6**, 2368–2374 (2006).
14. Loh, O. et al. Nanofountain-probe-based high-resolution patterning and single-cell injection of functionalized nanodiamonds. *Small* **5**, 1667–1674 (2009).
15. Weng, Z., Wang, J., Senthil, T. & Wu, L. Mechanical and thermal properties of abs/montmorillonite nanocomposites for fused deposition modeling 3d printing. *Mater. Des.* **102**, 276–283 (2016).
16. Mantihal, S., Prakash, S., Godoi, F. C. & Bhandari, B. Optimization of chocolate 3D printing by correlating thermal and flow properties with 3D structure modeling. *Innov. Food Sci. Emerg. Technol.* **44**, 21–29 (2017).
17. McCoul, D., Rosset, S., Schlatter, S. & Shea, H. Inkjet 3D printing of UV and thermal cure silicone elastomers for dielectric elastomer actuators. *Smart Mater. Struct.* **26**, 125022 (2017).
18. Edmondson, S., Osborne, V. L. & Huck, W. T. S. Polymer brushes via surface-initiated polymerizations. *Chem. Soc. Rev.* **33**, 14–22 (2004).
19. Fristrup, C. J., Jankova, K. & Hvilsted, S. Surface-initiated atom transfer radical polymerization—a technique to develop biofunctional coatings. *Soft Matter* **5**, 4623–4634 (2009).
20. Goh, T. K. et al. Nanoengineered films via surface-confined continuous assembly of polymers. *Small* **7**, 2863–2867 (2011).
21. Mertz, D. et al. ATRP-mediated continuous assembly of polymers for the preparation of nanoscale films. *Chem. Commun.* **47**, 12601 (2011).
22. Wong, E. H. H. et al. Phototriggered, metal-free continuous assembly of polymers for the fabrication of ultrathin films. *ACS Macro Lett.* **1**, 1020–1023 (2012).
23. Yeow, J., Chapman, R., Gormley, A. J. & Boyer, C. Up in the air: oxygen tolerance in controlled/living radical polymerisation. *Chem. Soc. Rev.* **47**, 4357–4387 (2018).
24. Piola, L., Nagra, F. & Nolan, S. P. Olefin metathesis in air. *Beilstein J. Org. Chem.* **11**, 2038–2056 (2015).
25. Dinger, M. B. & Mol, J. C. Degradation of the first-generation grubbs metathesis catalyst with primary alcohols, water, and oxygen. formation and catalytic activity of ruthenium(II) monocarbonyl species. *Organometallics* **22**, 1089–1095 (2003).
26. Dinger, M. B. & Mol, J. C. Degradation of the second-generation grubbs metathesis catalyst with primary alcohols and oxygen – isomerization and hydrogenation activities of monocarbonyl complexes. *Eur. J. Inorg. Chem.* **2003**, 2827–2833 (2003).
27. Lerum, M. F. Z. & Chen, W. Surface-initiated ring-opening metathesis polymerization in the vapor phase: an efficient method for grafting cyclic olefins with low strain energies. *Langmuir* **27**, 5403–5409 (2011).
28. Seehof, N., Grutke, S. & Risse, W. Selective reaction with exo-isomers in ring-opening olefin metathesis polymerization (ROMP) of fluoroalkyl-substituted norbornene derivatives. *Macromolecules* **26**, 695–700 (1993).

29. Pollino, J. M., Stubbs, L. P. & Weck, M. Living ROMP of exo -norbornene esters possessing Pd II SCS pincer complexes or diaminopyridines. *Macromolecules* **36**, 2230–2234 (2003).
30. Lutz, J.-F. Polymerization of Oligo(Ethylene Glycol) (Meth)acrylates: toward new generations of smart biocompatible materials. *J. Polym. Sci. Part Polym. Chem.* **46**, 3459–3470 (2008).
31. Lin, C.-C. & Anseth, K. S. PEG hydrogels for the controlled release of biomolecules in regenerative medicine. *Pharm. Res.* **26**, 631–643 (2009).
32. Zhu, J. Bioactive modification of poly(Ethylene Glycol) hydrogels for tissue engineering. *Biomaterials* **31**, 4639–4656 (2010).
33. Pattison, T. G. et al. Growing patterned, cross-linked nanoscale polymer films from organic and inorganic surfaces using ring-opening metathesis polymerization. *ACS Appl. Mater. Interfaces* **12**, 4041–4051 (2020).
34. Voinov, O. V. Hydrodynamics of wetting. *Fluid Dyn.* **11**, 714–721 (1976).
35. Cox, R. G. The dynamics of the spreading of liquids on a solid surface. Part 1. viscous flow. *J. Fluid Mech.* **168**, 169–194 (1986).
36. Erickson, D., Blackmore, B. & Li, D. An energy balance approach to modeling the hydrodynamically driven spreading of a liquid drop. *Colloids Surf. Physicochem. Eng. Asp.* **182**, 109–122 (2001).
37. Jang, J.-W. et al. Generation of metal photomasks by dip-pen nanolithography. *Small* **5**, 1850–1853 (2009).
38. Ma, X. et al. Size-tunable, highly sensitive microelectrode arrays enabled by polymer pen lithography. *Soft Matter* **13**, 3685–3689 (2017).
39. Ma, H., Jiang, Z., Xie, X., Huang, L. & Huang, W. Multiplexed biomolecular arrays generated via parallel dip-pen nanolithography. *ACS Appl. Mater. Interfaces* **10**, 25121–25126 (2018).
40. Piner, R. D., Zhu, J., Xu, F., Hong, S. & Mirkin, C. A. “Dip-Pen” nanolithography. *Science* **283**, 661–663 (1999).
41. Liu, G. & Xu, S. Nanometer scale fabrication of self-assembled monolayers: nanoshaving and nanografting. In *Inorganic Materials Synthesis*. (Eds. Winter, C. H., Hoffman, D. M.) Vol. 727, pp 199–208 (American Chemical Society, 1999).
42. Liu, J.-F., Cruchon-Dupeyrat, S., Garno, J. C., Frommer, J. & Liu, G.-Y. Three-dimensional nanostructure construction via nanografting: positive and negative pattern transfer. *Nano Lett.* **2**, 937–940 (2002).
43. Salaita, K. et al. Massively parallel dip-pen nanolithography with 55 000-pen two-dimensional arrays. *Angew. Chem. Int. Ed.* **45**, 7220–7223 (2006).
44. Bullen, D. et al. Parallel dip-pen nanolithography with arrays of individually addressable cantilevers. *Appl. Phys. Lett.* **84**, 789–791 (2004).

Acknowledgements

The authors would like to thank Mr. A. Tek at IBM for technical assistance in thermal polymer analysis, and Ms. Yunbo Zheng at UC Davis for helpful discussions, as well as Cytosurge AG for providing the SEM used in Fig. 1. T.G. Pattison would like to acknowledge the Australian Postgraduate Award and the University of Melbourne/IBM

Ph.D. Scholarship for funding this research. This work is also supported by National Science Foundation (USA, CHE-1808829, GYL) and Australian Research Council’s Discovery Program (DP17010432 and DP130101846, GGQ) as well as Future Fellowship Program (FT11010100411, GGQ).

Author contributions

T.G.P., S.W., R.D.M., G.L., and G.G.Q. helped in conceptualizing the study. T.G.P. carried out organic synthesis and characterization. T.G.P. and S.W. carried out 3D nanoprinting experiments and AFM analysis. T.G.P., S.W., R.D.M., G.L., and G.G.Q. assisted in manuscript preparation and editing.

Competing interests

The authors declare no competing interests.

Additional information

Supplementary information The online version contains supplementary material available at <https://doi.org/10.1038/s41467-022-29432-z>.

Correspondence and requests for materials should be addressed to Gang-yu Liu or Greg G. Qiao.

Peer review information *Nature Communications* thanks the anonymous reviewers for their contribution to the peer review of this work. Peer reviewer reports are available.

Reprints and permission information is available at <http://www.nature.com/reprints>

Publisher’s note Springer Nature remains neutral with regard to jurisdictional claims in published maps and institutional affiliations.



Open Access This article is licensed under a Creative Commons Attribution 4.0 International License, which permits use, sharing, adaptation, distribution and reproduction in any medium or format, as long as you give appropriate credit to the original author(s) and the source, provide a link to the Creative Commons license, and indicate if changes were made. The images or other third party material in this article are included in the article’s Creative Commons license, unless indicated otherwise in a credit line to the material. If material is not included in the article’s Creative Commons license and your intended use is not permitted by statutory regulation or exceeds the permitted use, you will need to obtain permission directly from the copyright holder. To view a copy of this license, visit <http://creativecommons.org/licenses/by/4.0/>.

© The Author(s) 2022